Cellular/Molecular

Ubiquitin-Specific Protease 2 in the Ventromedial Hypothalamus Modifies Blood Glucose Levels by Controlling Sympathetic Nervous Activation

Mayuko Hashimoto,[1,2]* Masaki Fujimoto,[3]* Kohtarou Konno,[5] Ming-Liang Lee,[4] Yui Yamada,[1]
Koya Yamashita,[3] Chitoku Toda,[4] Michio Tomura,[2] Masahiko Watanabe,[5] Osamu Inanami,[3] and
Hiroshi Kitamura[1]

[1]Laboratory of Veterinary Physiology, Department of Veterinary Medicine, School of Veterinary Medicine, Rakuno Gakuen University, Ebetsu
0698501, Japan, [2]Laboratory of Immunology, Faculty of Pharmacy, Osaka Ohtani University, Tondabayashi 5848450, Japan, [3]Laboratories of
Radiation Biology and, [4]Biochemistry, Faculty of Veterinary Medicine, Hokkaido University, Sapporo 0600808, Japan, and [5]Department of Anatomy
and Embryology, Graduate School of Medicine, Hokkaido University, Sapporo 0600808, Japan

Ubiquitin-specific protease 2 (USP2) participates in glucose metabolism in peripheral tissues such as the liver and skeletal muscles. However, the glucoregulatory role of USP2 in the CNS is not well known. In this study, we focus on USP2 in the ventromedial hypothalamus (VMH), which has dominant control over systemic glucose homeostasis. ISH, using a *Usp2*-specific probe, showed that *Usp2* mRNA is present in VMH neurons, as well as other glucoregulatory nuclei, in the hypothalamus of male mice. Administration of a USP2-selective inhibitor ML364 (20 ng/head), into the VMH elicited a rapid increase in the circulating glucose level in male mice, suggesting USP2 has a suppressive role on glucose mobilization. ML364 treatment also increased serum norepinephrine concentration, whereas it negligibly affected serum levels of insulin and corticosterone. ML364 perturbated mitochondrial oxidative phosphorylation in neural SH-SY5Y cells and subsequently promoted the phosphorylation of AMP-activated protein kinase (AMPK). Consistent with these findings, hypothalamic ML364 treatment stimulated AMPKα phosphorylation in the VMH. Inhibition of hypothalamic AMPK prevented ML364 from increasing serum norepinephrine and blood glucose. Removal of ROS restored the ML364-evoked mitochondrial dysfunction in SH-SY5Y cells and impeded the ML364-induced hypothalamic AMPKα phosphorylation as well as prevented the elevation of serum norepinephrine and blood glucose levels in male mice. These results indicate hypothalamic USP2 attenuates perturbations in blood glucose levels by modifying the ROS–AMPK–sympathetic nerve axis.

Key words: hypothalamus; mitochondria; reactive oxygen species; ubiquitin-specific protease 2; ventromedial hypothalamus

---

Significance Statement

Under normal conditions (excluding hyperglycemia or hypoglycemia), blood glucose levels are maintained at a constant level. In this study, we used a mouse model to identify a hypothalamic protease controlling blood glucose levels. Pharmacological inhibition of USP2 in the VMH caused a deviation in blood glucose levels under a nonstressed condition, indicating that USP2 determines the set point of the blood glucose level. Modification of sympathetic nervous activity accounts for the USP2-mediated glucoregulation. Mechanistically, USP2 mitigates the accumulation of ROS in the VMH, resulting in attenuation of the phosphorylation of AMPK. Based on these findings, we uncovered a novel glucoregulatory axis consisting of hypothalamic USP2, ROS, AMPK, and the sympathetic nervous system.

Introduction

Hypothalamic nuclei regulate glucose metabolism by modifying the autonomous nervous system and endocrine system (Berthoud and Morrison, 2008; Seoane-Collazo et al., 2015). When certain hypothalamic nuclei are electrically stimulated, sympathetic nerve fibers promote glycogenesis and glycogenolysis in the liver (Dubuc et al., 1982; Atrens et al., 1984). Sympathetic activation by the hypothalamus also positively and negatively influences circulating levels of glucoregulatory hormones, such as glucagon and insulin, respectively (Kalsbeek et al., 2010). Among several nuclei present

in the hypothalamus, the ventromedial hypothalamus (VMH) activates sympathetic nerves that innervate the liver and brown adipose tissue (Shimazu, 1981). Accordingly, photogenetic activation of VMH neurons potentiates sympathetic activity, resulting in an acceleration of glycogenolysis in the liver (Meek et al., 2016; Coutinho et al., 2017). Despite these previous studies, the molecules involved in the VMH-modulated sympathetic activation are still relatively unknown.

In eukaryotic cells, AMP-activated protein kinase (AMPK) is a key regulatory enzyme for cellular energy usage (Carling, 2017). Phosphorylation of AMPK is tightly modulated by the cellular nutritional state. When intracellular ATP is excessively consumed, accumulated AMP and ADP bind to the cystathionine β-synthase domain of AMPKγ and trigger phosphorylation of AMPKα (Jeon, 2016). In addition to this cellular role, hypothalamic AMPK is also known to be a regulator of systemic energy metabolism (Hirschberg et al., 2020; Liu et al., 2020). In VMH neurons, AMPK facilitates depolarization by opening and closing cystic fibrosis transmembrane conductance regulator channels and two-pore-domain potassium channels, respectively. Eventually, the depolarization of VMH neurons yields sympathetic activation in a voltage-gated calcium-channel-dependent manner (Coutinho et al., 2017). In accordance, blockage of hypothalamic AMPK causes hypoglycemia because of aberrant activation of the sympathetic nervous system (Fryer and Carling, 2005). Thus, adequate AMPK activation in the hypothalamus appears to be required for the maintenance of normal blood glucose levels. Previously, AMPK was postulated to be activated by ROS in hypothalamic neurons (Finley, 2019). ROS potentially decreases the mitochondrial membrane potential (Shanmughapriya et al., 2015), leading to decrements in ATP biosynthesis and the resultant AMPK phosphorylation (Hinchy et al., 2018). Additionally, ROS accelerates oxidation and S-glutathionylation at the C299 and C304 residues of AMPKα, resulting in an augmentation of the phosphorylation at T172 of AMPKα (Zmijewski et al., 2010).

Ubiquitination and deubiquitination are reversible processes that modulate the function of target proteins (Swatek and Komander, 2016). Ubiquitin-specific protease 2 (USP2), one of the deubiquitinating enzymes (DUBs), is expressed in a wide variety of tissues (Gousseva and Baker, 2003; Kitamura et al., 2013; Hashimoto et al., 2021) and plays a pivotal role in various cellular responses (Kitamura and Hashimoto, 2021), such as proliferation (Shi et al., 2011; Magiera et al., 2017), cell death (Priolo et al., 2006), and cytokine production (Kitamura et al., 2013, 2017). With regard to the function of USP2 in the CNS, *Usp2* knock-out mice had impaired brain-associated responses, including motor coordination, formation of working memory, and sensory-motor gating (Srikanta et al., 2021). In the hypothalamus, USP2 is one of the core components of the clock/brain and muscle Arnt-like protein 1 (BMAL1) complex in the suprachiasmatic nucleus (SCN; Scoma et al., 2011). In this nucleus, USP2 modulates circadian rhythm by digesting polyubiquitin chains on BMAL1 and the clock modulator, which is period (Scoma et al., 2011). Despite these pioneer studies, there is limited information about other regulatory roles of hypothalamic USP2. Because USP2 is upregulated in the hypothalamus of hypoglycemic mice (Mastaitis et al., 2005), a putative glucoregulatory role of USP2 can be postulated.

To date, several chemical inhibitors of USP2 have been identified (Davis et al., 2016; Chuang et al., 2018; Tomala et al., 2018). ML364 is currently the only commercially available USP2 inhibitor. Additionally, ML364 is applicable for *in vivo* studies (Zhao et al., 2018; He et al., 2019). In this study, we attempt to uncover the glucoregulatory roles of USP2 in VMH neurons using ML364 treatment.

Materials and Methods

Animals. Male C57BL/6N mice were purchased from Japan SLC (http://www.jslc.co.jp/english/animals/mouse.php#mouse-cat-01). Mice were maintained under a 12 h light/dark cycle and allowed to obtain food and water *ad libitum*.

VMH cannulation was performed as previously described (Toda et al., 2016). At 8–12 weeks old, mice were intraperitoneally injected with medetomidine (300 µg/kg; Meiji Seika Pharma), midazolam (4 mg/kg; Fuji Pharma), and butorphanol (5 mg/kg; Meiji Seika Pharma) for anesthesia and then placed on a stereotaxic instrument (Narishige International). A guide cannula (P1 Technologies) was inserted 1.4 mm posteriorly, 0.4 mm laterally, and 5.8 mm ventrally from the bregma. In some experiments, we inserted cannula into regions adjacent to the VMH. Meloxicam (4 mg/kg; Boehringer Ingelheim) was used for analgesia. After 7 d of recovery, 200 nl of ML364 (20 ng/head; MedChemExpress) or vehicle (PBS containing 5% BSA) was administered through the internal cannula (P1 Technologies). In some experiments, 200 nl of trolox (50 ng/head; Fujifilm Wako Pure Chemical) or vehicle (PBS containing 5% BSA) were administrated to the VMH 30 min before the ML364 or vehicle treatment. Two hundred nanoliters of Compound C (CC; 8 pg/head; MedChemExpress) or vehicle (PBS containing 5% BSA) was injected into the VMH 1 h before the ML364 or vehicle treatment. To elicit hypoglycemia, mice were given insulin (1 unit/kg, i.p.; Eli Lilly). Food intake per unit time was calculated by measuring the amount of pellets in the vessel before and after the ML364 or vehicle treatment. The location of the cannula was verified by injection of 200 nl of Hoechst 33342 (5 µg/ml; Thermo Fisher Scientific) through the cannula. The brains were immediately collected and frozen on powdered dry ice to prepare 20-µm-thick frozen sections. Images of the sections were captured using an IX71 fluorescence microscope (Olympus) connected to a DP73 cooling charged-coupled device camera (Olympus).

All animal experiments were approved by the Animal Experimentation Committee of Rakuno Gakuen University (Approval Nos. VH17A27, VH21A14, and VH21A15). Care and management of experimental animals and experimental operations were conducted in compliance with the guidelines for animal experiments of Rakuno Gakuen University.

Cell culture. The human neuroblastic cell line SH-SY5Y was obtained from the European Collection of Authenticated Cell Cultures. The cells were grown in DMEM-Ham F12 medium mixture (1:1; Nacalai Tesque) supplemented with 4.5 g/L glucose and 15% FBS. The cells were incubated with ML364 (final concentration 10 µM or 5.2 µg/ml) or vehicle (DMSO; final concentration 2 mM) for 2 h. In some experiments, we treated the cells with the ROS scavenger trolox (final concentration 100 µM or 25 µg/ml), *N*-acetyl cysteine (NAC; final concentration 20 mM or 2.72 mg/ml) or vehicle (PBS) for 2 h before ML364 or vehicle treatment.

Histologic analysis. For chromogenic ISH, brains were fixed with 4% paraformaldehyde by transcardial perfusion under sodium pentobarbital (100 mg/kg i.p.; Kyoritu Seiyaku) anesthesia. After extraction from the skull, the brains were immersed in 4% paraformaldehyde for 3 d and then immersed in 30% sucrose. The tissues were then embedded in optimum cutting temperature compound (Sakura Finetek) and sectioned into 50-µm-thick slices by cryostat. For fluorescent ISH, freshly isolated brains were frozen on powdered dry ice to prepare 5-µm-thick frozen sections.

To generate *Usp2* cRNA probes, a mouse *Usp2* cDNA fragment (accession no. NM_198091, GenBank; corresponding with the 44 000,429-44 005,159 bp of the mouse genome version GRCm 38.p2) was cloned into a pBluescriptII plasmid vector (Addgene). For sense and antisense probes for *Usp2* mRNA, the plasmid was digested with BamHI (New England Biolabs) or HindIII (New England Biolabs). DIG-labeled *Usp2* cRNA probes and fluorescein-labeled *Usp2* cRNA probes were generated by *in vitro* transcription using DIG RNA Labeling Mix (Roche Diagnostics) and Fluorescein RNA Labeling Mix (Roche Diagnostics), respectively. The excitatory amino acid transporter 1 (*Eaat1*) probe has been described previously (Castañeda-Cabral et al., 2020).

Chromogenic and fluorescent ISH were performed as previously reported (Konno et al., 2014). Sections were processed as follows: acetylation with 0.25% acetic anhydride in 100 µM triethanolamine-hydrochloride, pH

8.0, for 10 min and prehybridization for 1 h in hybridization buffer (50% formamide, 50 mM tris-hydrochloride, pH 7.5, 0.02% Ficoll, 0.02% polyvinylpyrrolidone, 0.02% bovine serum albumin, 600 μM sodium chloride, 200 μg/ml of tRNA, 1 mM EDTA, and 10% dextran sulfate). Hybridization was performed at 63.5°C for 12 h in hybridization buffer supplemented with cRNA probes at a dilution of 1:1000. Posthybridization washing was done at 61°C successively with 5× standard sodium citrate (SSC) for 30 min, 4× SSC containing 50% formamide for 40 min, 2× SSC containing 50% formamide for 40 min, and 0.1× SSC for 30 min. Sections were incubated at room temperature in NaCl-Tris-EDTA (NTE) buffer (500 mM sodium chloride, tris-hydrochloride, pH 7.5, and 5 mM EDTA) for 20 min, 20 mM iodoacetamide in NTE buffer for 20 min, and TNT buffer (100 mM tris-hydrochloride, pH 7.5, 150 mM sodium chloride, and 0.1% Tween 20) for 20 min. Subsequently, the sections were blocked with a blocking solution [100 mM tris-hydrochloride, pH 7.4, 1% blocking reagent (Roche Diagnostics), 4% sheep serum, 150 mM sodium chloride, and 0.5% Tween 20] for 30 min.

For chromogenic detection, the sections were treated with alkaline phosphatase-conjugated sheep anti-DIG antibody (1:500; Roche Diagnostics) for 90 min and incubated in a detection buffer (100 μM tris-hydrochloride, pH 10.5, 100 mM sodium chloride, 50 mM magnesium chloride) containing 200 μM nitro blue tetrazolium/5-bromo-4-chloro-3'-indolyl phosphate (Roche Diagnostics) for 12 h. Images of chromogenic ISH results were captured using an optical microscope (BZ-9000; Keyence).

For fluorescence detection, the sections were incubated with peroxidase-conjugated anti-fluorescein antibody (1:1000; Roche Diagnostics) for 1 h and then incubated with fluorescein isothiocyanate-conjugated tyramide signal amplification plus solution (PerkinElmer) at 40°C for 30 min. After vigorous washing with TNT buffer, the sections were immersed in 1% hydrogen peroxide solution for 30 min. Subsequently, the sections were sequentially treated with peroxidase-conjugated anti-DIG antibody (1:1000; Roche Diagnostics) for 1 h and cyanine 3-tyramine signal amplification plus amplification solution (PerkinElmer) for 10 min. After halting the amplification by washing with TNT buffer, the sections were blocked with 10% donkey serum for 20 min and incubated with a NeuN antibody (1:1000; catalog #MAB377, Merck Millipore) for 2 h. After extensive washing with PBS, the sections were treated with Alexa Fluor 647 conjugated donkey anti-mouse IgG (1:200; Thermo Fisher Scientific) for 2 h. The images were captured using a confocal laser scanning microscope (FV1000, Olympus). In some experiments, we calculated the proportion of *Usp2* mRNA$^+$ area in NeuN$^+$ or *Eaat1* mRNA$^+$ areas in four microscopic views (magnification, 200-fold) of parenchymal region of the VMH for each mouse.

Blood tests. Blood was collected from the tail vein at 0, 30, 60, 90, and 120 min after intra-VMH administration of ML364 or vehicle. Blood glucose was measured using the Test Wako Kit (Fujifilm Wako Pure Chemical). Serum was isolated from blood samples by centrifugation at 3000 × *g* for 15 min. Serum norepinephrine, insulin, and corticosterone concentrations were measured using a Norepinephrine ELISA kit (ImmuSmol), a Mouse Insulin ELISA kit (Fujifilm Wako Pure Chemical), and a Corticosterone ELISA kit (Arbor Assays), respectively.

Hepatic glycogen phosphorylase activity. The livers were homogenized in an extraction buffer containing the following (in mM): 20 tris-hydrochloride, pH 7.2, 250 sucrose, 50 sodium fluoride, 4 EDTA, and 0.5 dithiothreitol, using a dounce tissue homogenizer. After centrifugation at 3300 × *g* for 7 min, the supernatant was diluted 100-fold in a dilution solution of 40 mM sodium citrate, pH 6.5, and 40 mM *β*-mercaptoethanol. An equal volume of substrate solution (1% glycogen and 2 mM adenosine monophosphate; Fujifilm Wako Pure Chemical) was added to the samples, which were then incubated at 37°C for 2 min. Subsequently, an equal volume of 40 mM disodium D-glucose 6-phosphate (Fujifilm Wako Pure Chemical) was added to the samples and further incubated at 37°C for 10 min. After the addition of a 10-times volume of a molybdate solution (750 mM sulfurous acid and 100 mM ammonium molybdate) and a 10-times volume of 1-amino-2-naphthol-4-sulfonic acid solution containing the following (in mM): 40 sodium sulfite, 3 1-amino-2-naphthol 4-sulfonic acid, 700 sodium bisulfate, the

reaction mixture was incubated for 10 min. The reaction was stopped by adding an equal volume of 2 M triethanolamine. Absorbance at 780 nm was measured using an iMark microplate reader (Bio-Rad).

Western blotting analysis. The VMH-containing hypothalamic area was cut out using a blade according to a previously published protocol (Gagnidze et al., 2013). Western blotting analysis was performed as previously described (Kitamura et al., 2017). Briefly, protein was extracted from tissues or cells with RIPA buffer [50 mM tris-hydrochloride, pH 7.6, 150 mM sodium chloride, 1% Nonidet P-40, 0.5% sodium deoxycholate, 0.1% SDS, 1 mM EDTA, protease inhibitor cocktail (Merck Millipore)]. After boiling samples in the presence of 4% SDS, the samples were loaded into a 10% SDS-polyacrylamide gel and transferred to a polyvinylidene difluoride membrane (Merck Millipore). The membranes were then blocked with Blocking One reagent (Nacalai Tesque) at room temperature for 1 h, and reacted with anti-phosphorylated AMPKα antibody (pAMPKα; 1:2000, catalog #2535; Cell Signaling Technology), anti-total AMPKα antibody (1:2000; catalog #2532; Cell Signaling Technology), or GAPDH antibody (1:5000, catalog #sc-47724; Santa Cruz Biotechnology) in a Can Get Signal enhancer solution (Toyobo) at 4°C overnight. The membranes were subsequently incubated with horseradish peroxidase-conjugated anti-rabbit IgG (1:5000; catalog #7074S; Cell Signaling Technology) at room temperature for 3 h. Immunologic signals were visualized with a Chemi Lumi One Super Kit (Nacalai Tesque) and monitored using the EZ Capture system (Atto).

Lactate dehydrogenase assay. The cytotoxicity of ML364 was evaluated using a lactate dehydrogenase (LDH) Assay kit (Dojindo, Kumamoto). The assays used 1×10^4 cells/well in a 96-well plate. Assays were performed according to the instructions provided by the manufacturer.

Intracellular ATP content. Intracellular ATP content was measured using an ATP measurement solution (Toyo B-Net) as previously described (Hashimoto et al., 2019). SH-SY5Y cells (1×10^4 cells per well in a 96-well plate) were preincubated at 37°C for 12 h. Then, an equal volume of ATP measurement solution was added to the culture medium and mixed vigorously using a plate shaker for 1 min. The chemiluminescent signal was measured using a Victor Nivo Multimode Microplate Reader (PerkinElmer).

Mitochondria isolation and mitochondrial respiratory chain complex activities. Three million SH-SY5Y cells were seeded in a 10 cm dish and incubated for 12 h. Subsequently, they were treated with ML364 or vehicle for 2 h. Then, mitochondria were isolated from the cells using a Mitochondria Isolation kit (Abcam) according to the protocol of the manufacturer. Activities of the mitochondrial complexes were measured using a Victor Nivo Multimode Microplate Reader at 30°C as previously described, with some modifications (Yamamori et al., 2012; Hashimoto et al., 2019).

Complex I activity was determined as the inhibitable rate of reduced nicotinamide adenine dinucleotide (NADH) oxidation by rotenone. Isolated mitochondria were incubated in 25 mM potassium dihydrogen phosphate, pH 7.2, 5 mM magnesium chloride, 0.2% BSA, 65 μM coenzyme Q1 (Sigma Aldrich), 2 μg/ml antimycin A, and 2 mM potassium cyanide for 5 min. Then, 325 μM NADH with either 2 μg/ml rotenone or DMSO was added to the mitochondrial suspension. Absorbance at 340 nm was measured every 30 s for 20 min.

Complex II activity was measured by monitoring 2,6-dichlorophenolindophenol (DCPIP) reduction. Mitochondria were incubated with 25 mM potassium dihydrogen phosphate, pH 7.2, 20 mM sodium succinate, 5 mM magnesium chloride, 2 mM potassium cyanide, 65 μg/ml coenzyme Q1, 2 μg/ml antimycin A, and 10 μg/ml rotenone. Subsequently, 150 μM DCPIP (Sigma-Aldrich) was added to the mitochondrial suspension. Absorbance at 600 nm was measured every 30 s for 20 min.

Complex III activity was measured by the inhibitable rate of oxidative cytochrome *c* (III) by antimycin A. Mitochondria were incubated in 50 mM potassium dihydrogen phosphate, pH 7.2, 0.1% BSA, 100 μM EDTA, 2 mM potassium cyanide, and 35 μM coenzyme Q1 for 5 min. Following incubation, 60 μM oxidative cytochrome *c* (Sigma-Aldrich) and either 2 μg/ml antimycin A or DMSO were added to the mitochondrial suspension. Absorbance at 550 nm was measured every 30 s for 20 min.

Complex IV activity was measured by the rate of cytochrome c (II) oxidation. Cytochrome c (II) was reduced by incubation with 500 μM dithiothreitol for 15 min before measurement. Mitochondria were incubated with a solution containing 25 mM potassium dihydrogen phosphate, pH 7.2, and 0.45 mM n-dodecyl-β-D-maltoside for 5 min. Then, 15 μM reduced cytochrome c (II) was added to the mitochondrial suspension. Absorbance at 550 nm was measured every 30 s for 20 min.

F_0F_1 ATPase/complex V activity was measured by monitoring the decrease of NADH. Mitochondria were incubated with the following (in mM): 50 4-(2-hydroxyethyl)−1-piperazineethanesulfonic acid, 3 magnesium chloride, 50 potassium cyanide, 0.2 EDTA, 2 phosphoenolpyruvic acid, and 100 μM rotenone, 10 units/ml lactate dehydrogenase (Oriental Yeast), and 10 units/ml pyruvate kinase (MP Biomedicals) for 5 min, and then treated with 2 mM ATP and 500 μM NADH in the presence or absence of 10 μg/ml oligomycin (Fujifilm Wako Pure Chemical). Absorbance at 340 nm was measured every 30 s for 20 min.

Mitochondrial membrane potential. The mitochondrial membrane potential was assessed using an MT-1 MitoMP Detection kit (Dojindo). SH-SY5Y cells (2 × 10^5 cells in a well of a 24-well plate) were treated with an MT-1 solution (1:1000) for 30 min. After washing with warm PBS, the cells were monitored using a FACSVerse (BD Biosciences).

ROS detection. Accumulation of mitochondrial ROS in SH-SY5Y cells were visualized with MitoSOX Red Superoxide Indicator (Thermo Fisher Scientific). The cells (2 × 10^5 cells/well in a 24-well plate) were treated with MitoSOX Red reagent (final concentration 5 μM) for 10 min. After washing with warm PBS, the cells were monitored using a FACSVerse.

ROS accumulation in the brain sections was evaluated using the dihydroethidium (DHE) staining method (Mo et al., 2019). Nonfixed frozen mouse brains cut into a thickness of 20 μm were incubated with DHE (5 μM; Fujifilm Wako Pure Chemical) at 37°C for 30 min. After staining the nuclei with Hoechst 33342 (5 μg/ml, Thermo Fisher Scientific), microscopic images were captured using a C2 laser scanning confocal microscope (Nikon) and analyzed using ImageJ software (Schneider et al., 2012). The threshold of signal intensity was set at 120, and the sum of areas exhibiting a stronger signal than the threshold value was calculated.

Statistical analysis. Descriptions of critical variables (e.g., number of animals and experiments) can be found in the figure legends. Statistical analysis was conducted using a Student's t test (Figs. 1H, 2C,E,F,J–L, 3), or one-way (Fig. 2B) or two-way (Figs. 2D, 4, 5, 6C–G) ANOVA using the KaleidaGraph software (Hulinks). For two-way ANOVA, the main effects of the two factors and their interaction are shown. Additionally, Tukey's test (Figs. 2D, 4, 5, 6C–G) and Dunnett's test (Fig. 2B) were used as *post hoc* tests for ANOVA.

The correlation coefficient between blood glucose level, blood insulin level, and hepatic phosphorylase activity in the same cohort study was calculated by a Pearson's correlation coefficient test using the KaleidaGraph software (Figs. 2G–I). When the p value was <0.05, we regarded it as a significant correlation between the indices.

Results

Usp2 transcripts are distributed in VMH neurons
To elucidate the localization of *Usp2* mRNA in the mouse brain, we performed chromogenic ISH using a *Usp2* cRNA probe. In
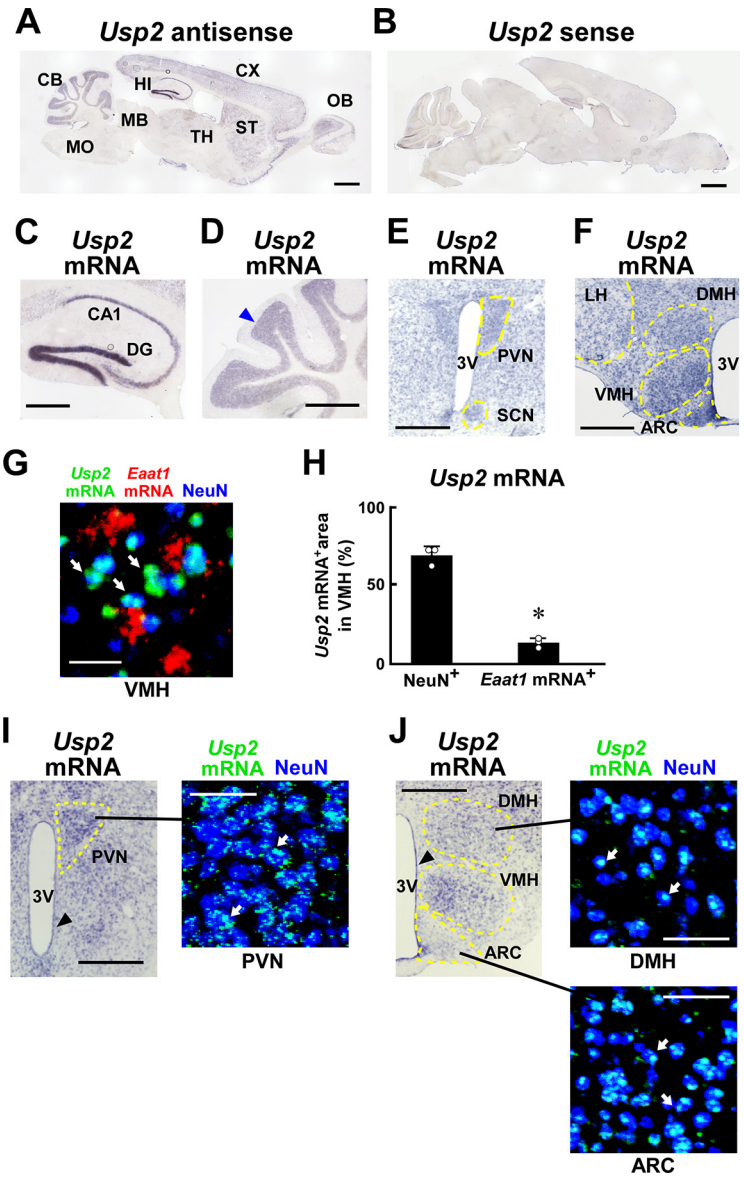

Figure 1. Expression of *Usp2* mRNA in the mouse brain. *A–G, I, J*, Chromogenic (*A–F, I, J*) and fluorescent (*G, I, J*) ISH using antisense (*A, C–G, I, J*) or sense (*B*) probes for *Usp2* transcripts; sagittal (*A–D*) and coronal (*E–G, I, J*) sections of adult mouse brains are shown, with highly magnified images of the hippocampus (*C*), cerebellar (*D*), and hypothalamic (*E–G, I, J*) regions. *G, I, J*, Combinatory technique of fluorescent ISH (*Usp2* mRNA and *Eaat1* mRNA) and immunofluorescence detection (NeuN) in VMH (*G*), PVN (*I*), and ARC and DMH (*J*). *H*, Distribution of *Usp2* mRNA⁺ to NeuN⁺ or *Eaat1* mRNA⁺ cells in the parenchymal region of the VMH. The proportion of *Usp2* mRNA⁺ area colocalized with NeuN⁺ or *Eaat1* mRNA⁺ were calculated. *I, J*, Right, Lower and higher magnification of hypothalamic nuclei. *E, F, I, J*, The hypothalamic nuclei are surrounded by yellow dashed lines. Blue arrowhead indicates the cerebellar granular layer (*D*). *G, I, J*, Arrows indicate *Usp2* mRNA signal on NeuN⁺ neurons. Black arrowheads indicate *Usp2* mRNA signal on ependymal cells (*I, J*). CB, Cerebellum; CX, cortex; HI, hippocampus; LH, lateral hypothalamus; MB, midbrain; MO, medulla oblongata; OB, olfactory bulb; ST, striatum; TH, thalamus; 3V, third ventricle. Scale bars: *A, B*, 1 mm; *C, F*, and *I, J* (left), 500 μm; *G*, 20 μm; *I, J* (right), 50 μm. Representative images of three experiments are shown. Data are shown as mean ± SD of three mice (*H*); *p < 0.05 versus NeuN⁺ cells calculated by Student's t-test (*H*).

sagittal sections of the mouse brain, the positive signals for *Usp2* mRNA were distributed in various areas, with higher levels in the telencephalon and cerebellum (Fig. 1A). Because the sense probe for the *Usp2* transcript did not give any significant signal (Fig. 1B), the *Usp2* cRNA probe can be considered specific. Confirming results previously published by Li et al. (2018), *Usp2* mRNA was highly expressed in the CA1 and dentate gyrus (DG) regions of the hippocampus (Fig. 1C). Additionally, the
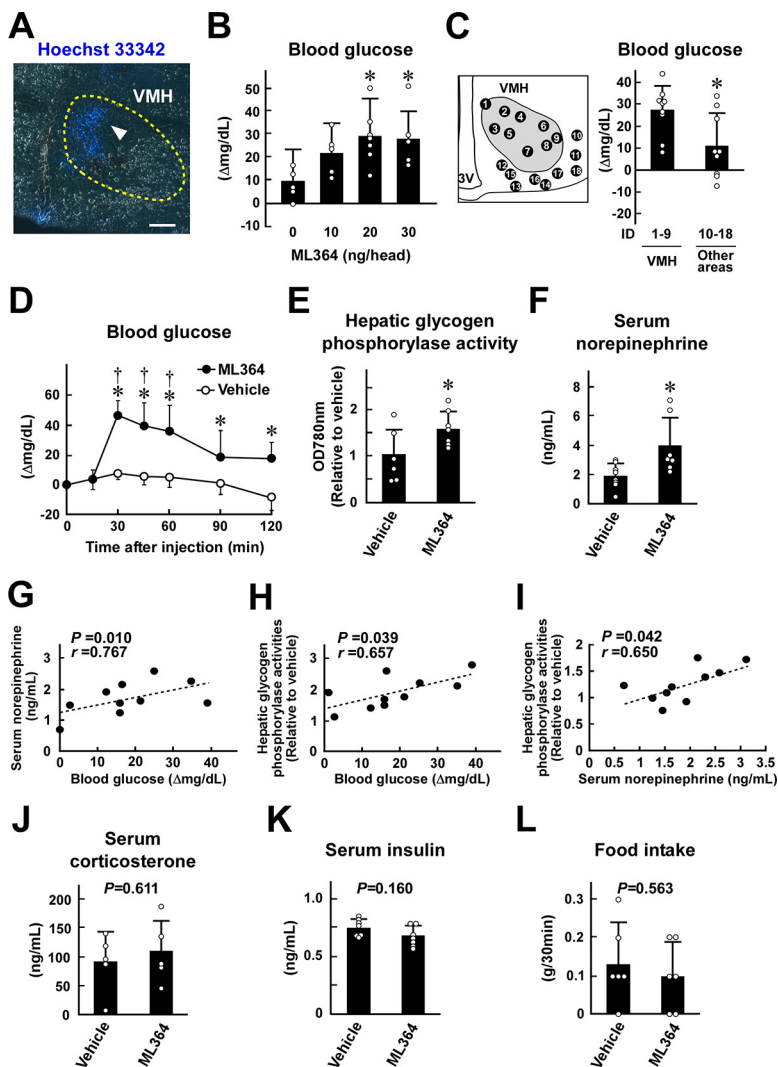
Figure 2. Alteration of peripheral blood glucose mobilization after intra-VMH administration of ML364. *A*, Location of intra-VMH cannula. After injection of Hoechst 33342 (5 μg/ml, 200 nl) into VMH, the hypothalamic section was observed. A representative image of 10 mice is shown. White arrowhead indicates the Hoechst 33342-stained area. The VMH is surrounded by a yellow dashed line. *B–L*, After injection of ML364 (10–30 ng, *B*; 20 ng, *C–L*) or vehicle (5% BSA-supplemented PBS) into the VMH (*B–L*) or adjacent areas (*C*), blood (*B–D, G, H*), serum (*F, G, I–K*) and liver (*E, H, I*) were collected. Blood glucose level (*B–D*). Blood glucose levels were determined 30 min after application of ML364 or vehicle (*B, C*). Schematic presentation of ML364 injection sites (left) and blood glucose level (right; *C*). Mouse individual numbers (IDs) are shown in the scheme and graph (*C*). Time course of changes in blood glucose level after injection of ML364 or vehicle (*D*). Injection time is regarded as 0 min (*D*). *E, F*, Hepatic glycogen phosphorylase activity (*E*) and serum concentrations of norepinephrine (*F*) 30 min after ML364 or vehicle injection. *G–I*, Correlation coefficient between blood glucose level, serum norepinephrine level, and hepatic glycogen phosphorylase activities 30 min after ML364 injection in the same cohort study. *J, K*, Serum corticosterone (*J*) and insulin (*K*) levels 30 min after ML364 or vehicle injection. *L*, Food intake during the 0–30 min after ML364 or vehicle administration. Data are shown as mean ± SD of five (*J*); five–seven (*B*); six (*D, L*); seven (*K*); six, seven (*E*); seven, eight (*F*); nine (*C*); 10 (*G–I*) mice. One-way ANOVA followed by Dunnett's test (*B*), two-way ANOVA followed by Tukey's test (*D*), and Student's *t* test (*C, E, F, J–L*) were performed. Correlation coefficients were calculated using Pearson's correlation coefficient test (*G–I*); *$p < 0.05$ versus vehicle-treated mice (*B–F*); †$p < 0.05$ versus 0 min (*D*). Correlation coefficients (*r*; *G–I*) or *p* values are also shown (*G–L*).

cerebellar granular layer exhibited intense hybridization signals (Fig. 1*D*). In the hypothalamus, *Usp2* mRNA was observed in various nuclei, such as the VMH, paraventricular nucleus (PVN), arcuate nucleus (ARC), dorsomedial hypothalamus (DMH), and lateral hypothalamus (Fig. 1*E,F*). Moreover, *Usp2* signals were also present in the SCN, as previously reported (Fig. 1*E*; Scoma et al., 2011).

We then attempted to specify the cell type expressing *Usp2* mRNA in the hypothalamus. In the VMH, $69.7 \pm 5.80\%$ of *Usp2* mRNA$^+$ signals were colocalized with NeuN$^+$ cells. By contrast,

only $13.7 \pm 3.23\%$ of *Usp2* mRNA$^+$ signals were detected in *Eaat1* mRNA$^+$ cells (Fig. 1*G,H*), which seem to be astrocytes (Shibata et al., 1997). The *Usp2* hybridization signal was also strongly detected in neurons of other hypothalamic nuclei, namely PVN (Fig. 1*I*), ARC (Fig. 1*J*), and DMH (Fig. 1*J*), as well as in ependymal cells along the third ventricle wall (Fig. 1*I,J*). These results indicate that in the hypothalamus, it is neurons that predominantly express USP2.

Chemical inhibition of USP2 in the VMH elevates blood glucose via sympathetic nervous activation

The VMH is a nucleus that is well documented as participating in systemic control of glucose metabolism (Coutinho et al., 2017). We focused on the glucoregulatory roles of USP2 in the VMH. We attempted to selectively inject a chemical inhibitor of USP2, ML364, into the VMH. To validate the location of the cannula, we specified the injected area in the hypothalamus by administration of a small amount (200 nl) of Hoechst 33342. As shown in Figure 2*A*, Hoechst-33342-derived blue fluorescence was only observed within the VMH of mice.

We next evaluated the effects of the intra-VMH injection of an USP2-selective chemical inhibitor on blood glucose levels. Injection of ML364 (20 or 30 ng) into the VMH significantly increased blood glucose levels 30 min after the injection ($p = 0.051$, one-way ANOVA; 20 ng vs 0 ng, $p = 0.013$; 30 ng vs 0 ng, $p = 0.036$; Dunnett's test; $n = 5–7$) whereas 10 ng of this reagent failed to increase blood glucose levels (10 ng vs 0 ng, $p = 0.145$; Dunnett's test; $n = 5$; Fig. 2*B*). Because the glucoregulatory effects were indistinguishable between 20 and 30 ng/head of ML364, we used 20 ng/head of ML364 in all further analyses. Although the intra-VMH administration of ML364 increased blood glucose levels, we cannot exclude the possibility that the injected ML364 affected the adjacent nuclei. Thus, we also measured blood glucose levels after ML364 injection to the VMH as well as the adjacent areas. As mentioned above, blood glucose levels exhibited a prominent increase in the VMH-treated mice 30 min after the injection, whereas the increase was limited in the other areas ($p = 0.018$ means of VMH-treated mice vs other-areas-treated mice, Student's *t*-test; $n = 9$; Fig. 2*C*). Hence, the VMH seems to be a site where blood glucose may be raised after treatment with ML364. Figure 2*D* represents the time course effects of intra-VMH administration of ML364 on blood glucose levels. Two-way ANOVA indicated that changes induced by treatment exhibited statistical significance ($p = 0.0002$; $n = 6$), whereas changes by time points displayed no statistical significance ($p = 0.051$; $n = 6$). No

interaction was detected between the indices ($F = 1.245$, $p = 0.294$). *Post hoc* testing showed that blood glucose levels had rapidly increased ($p = 0.000004$ vs 0 min; Tukey's test; $n = 6$) 30 min after injection of ML364 into the VMH, whereas vehicle-treated mice displayed negligible changes to their blood glucose levels ($p = 0.000004$ vs 0 min; Tukey's test; $n = 6$). The increase in blood glucose was more drastic in ML364-treated mice than in vehicle-treated mice ($p = 0.000001$, 0.000002, 0.000006, and 0.0032 vs vehicle-treated mice) at 30, 45, 60, and 90 min after the injection, respectively (Tukey's test; $n = 6$). Thereafter, the ML364-evoked increase in circulating glucose gradually decreased, although the significant increase was still present at 120 min ($p = 0.00005$ vs vehicle-treated mice; Tukey's test; $n = 6$).

Hepatic glycogenolysis is a determinant of the circulating glucose level. Accordingly, we measured glycogen phosphorylase activity in the liver 30 min after the administration of ML364. As shown in Figure 2E, intra-VMH administration of ML364 upregulated glycogen phosphorylase activity by ~1.6-fold compared with the vehicle-treated mice ($p = 0.048$; Student's t test; $n = 6–7$). Thus, inhibition of USP2 in the VMH raises blood glucose levels, at least in part, by accelerating hepatic glycogenolysis.

As the VMH controls peripheral glucose metabolism through the regulation of the sympathetic nervous system (Shimazu, 1981), we measured serum norepinephrine levels after intra-VMH administration of ML364. Thirty minutes after injection, ML364-treated mice exhibited higher (~2.0-fold) serum norepinephrine levels compared with vehicle-treated mice ($p = 0.020$; Student's t test; $n = 7–8$; Fig. 2F).

To confirm that the increase in blood glucose levels is related to sympathetic activation after ML364 injection, we assessed the correlation between blood glucose and serum norepinephrine levels in the same cohort study. Pearson's correlation coefficient analysis indicated that blood glucose levels had positive correlations with serum norepinephrine 30 min after ML364 injection ($r = 0.767$, $p = 0.010$, $n = 10$; Fig. 2G). In the same study, hepatic glycogen phosphorylase activity also showed a positive correlation with blood glucose levels ($r = 0.657$, $p = 0.039$, $n = 10$; Fig. 2H). Therefore, hepatic glycogen phosphorylase activity was correlated with the serum norepinephrine level ($r = 0.650$, $p = 0.042$, $n = 10$; Fig. 2I). These results collectively suggest that intra-VMH administration of ML364 evokes sympathetic activation leading to peripheral glucose mobilization.

We next measured blood levels of other glucoregulatory hormones. In contrast to norepinephrine, ML364 treatment failed to
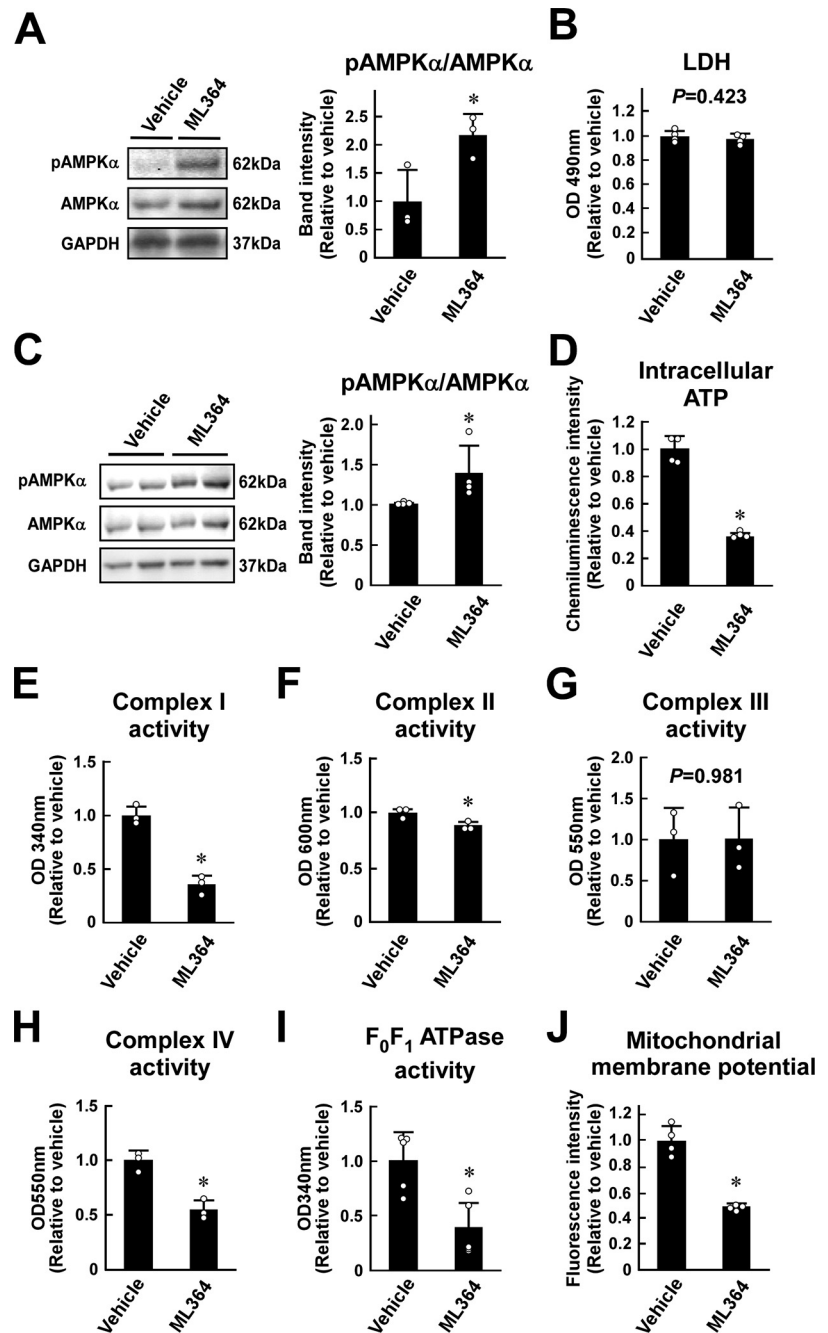
Figure 3. ML364 activates AMPK by inducing mitochondrial dysfunction. **A**, Western blot detection of pAMPKα and total AMPKα. Ratios of pAMPKα to AMPKα at 30 min after ML364 (20 ng) or vehicle (5% BSA-supplemented PBS) was delivered to the VMH of mice. **B–J**, Left, Representative immunoblot images. GAPDH was detected as a loading control. Representative images of three independent experiments are shown. Right, Semiquantitative band intensity data. Effects of ML364 (10 μM) on LDH content in the culture medium (**B**), AMPK phosphorylation (**C**), intracellular level of ATP (**D**), enzymatic activities of respiratory chain complexes (**E–I**), and mitochondrial membrane potential (**J**) in SH-SY5Y cells. SH-SY5Y cells were treated with ML364 (10 μM) or vehicle (2 mM DMSO) for 2 h. Semiquantitative band intensity data were analyzed as in **A** (**C**). Intracellular ATP content was normalized to cell numbers and is represented as relative to the mean value of the vehicle-treated cells (**D**). Mitochondria isolated from ML364-treated or vehicle-treated cells were subjected to colorimetric assays for complexes I (**E**), II (**F**), III (**G**), IV (**H**), and F$_0$F$_1$ ATPase/complex V (**I**) activities. The net activity of complexes I, III, and F$_0$F$_1$ ATPase was calculated by subtracting the background activity of cells treated with the respective inhibitors (2 μg/ml rotenone, 2 μg/ml antimycin A, and 10 μg/ml oligomycin for complexes I, III, and F$_0$F$_1$ ATPase, respectively). Values are represented as relative to those observed in vehicle-treated cells. The mitochondrial membrane potential was evaluated by staining with MT-1 solution (**J**). Fluorescence intensity of the cells was analyzed using a flow cytometer. After subtraction of the fluorescence intensity of unstained cells, the median fluorescent signal values were calculated. Data are shown as mean $\pm$ SD of three mice (**A**) or three (**E–H**), four (**B–D, J**), and five (**I**) cell experiments. For statistical analyses, Student's t test was performed; *$p < 0.05$ versus vehicle-treated mice (**A**) or vehicle-treated SH-SY5Y cells (**B–F, H–J**); p values are shown (**B, G**).
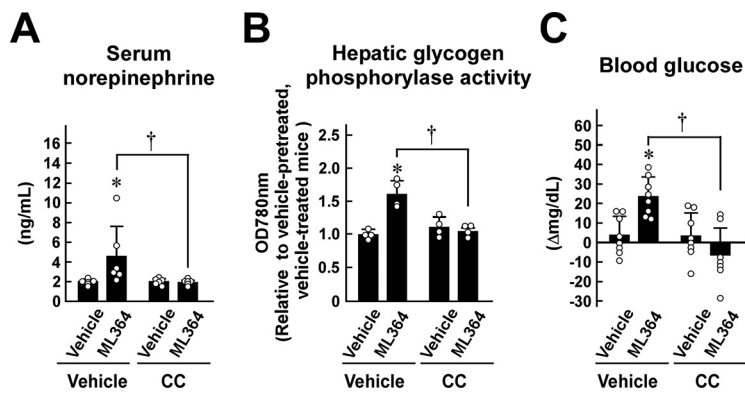
Figure 4. Involvement of hypothalamic AMPK in the ML364-elicited peripheral glucose control. CC (8 pg) or vehicle (5% BSA-supplemented PBS) was applied to the VMH 1 h before administration of ML364 (20 ng) or vehicle (5% BSA-supplemented PBS). *A–C*, Serum (*A*), liver (*B*), and blood (*C*) were collected before (*C*) and 30 min after (*A–C*) administration of ML364 or vehicle. Serum norepinephrine levels (*A*), hepatic glycogen phosphorylase activity (*B*), and blood glucose levels (*C*) were measured. Values are represented as relative to vehicle-pretreated, vehicle-treated mice (*B*). Data are shown as mean ± SD of four (*B*), six (*A*), and eight (*C*) mice. Two-way ANOVA followed by Tukey's test as a *post hoc* test was conducted as statistical analysis; *$p < 0.05$ versus vehicle-treated mice; †$p < 0.05$ versus vehicle-pretreated mice.
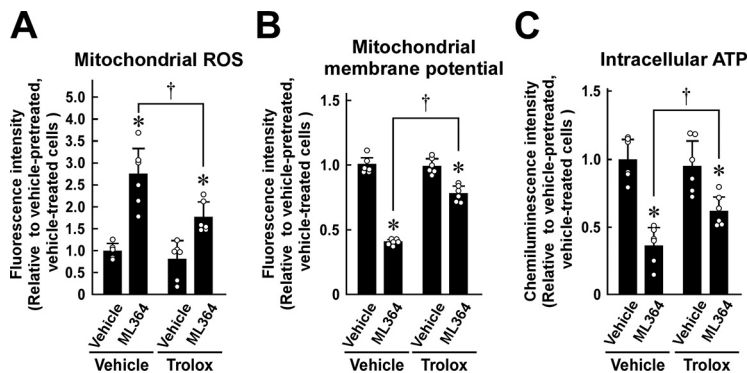

Figure 5. Involvement of ROS accumulation in SH-SY5Y cells in the ML364-elicited mitochondrial dysfunction. *A–C*, Following 2 h incubation with ML364 (10 μM) or vehicle (2 mM DMSO) in the presence or absence of trolox (100 μM), accumulation of mitochondrial ROS (*A*), mitochondrial membrane potential (*B*), and intracellular ATP level (*C*) were measured. After subtraction of the fluorescence intensity of unstained cells, the median fluorescent signal values were calculated (*A*, *B*). Intracellular ATP content was normalized to cell numbers (*C*). Values are represented as relative to vehicle-pretreated, vehicle-treated cells. Data are shown as mean ± SD of six experiments. Two-way ANOVA followed by Tukey's test as a *post hoc* test was conducted as statistical analysis; *$p < 0.05$ versus vehicle-treated cells; †$p < 0.05$ versus vehicle-pretreated cells.

affect circulating corticosterone levels (1.2-fold, $p = 0.611$; Student's *t*-test; $n = 6$; Fig. 2*J*). Likewise, ML364 negligibly influenced serum insulin levels (0.92-fold, $p = 0.160$; Student's *t*-test; $n = 7$–8; Fig. 2*K*). ML364 did not modulate food intake within the 30 min after ML364 administration (0.75-fold, $p = 0.563$; Student's *t*-test; $n = 6$, Fig. 2*L*). In line with these findings, sympathetic activation could be ascribed to hyperglycemia after injection of ML364 into the VMH.

ML364 activates AMPK by inducing mitochondrial impairment

Previous reports demonstrated that AMPK in VMH neurons contributes to the sympathetic activation that leads to hepatic glycogenolysis (Ikegami et al., 2013; Tanida et al., 2015). Thus, we hypothesized that AMPK mediates the ML364-elicited hyperglycemia. To assess this, we monitored the phosphorylation state of hypothalamic AMPKα after injection of ML364 into the

VMH. As shown in Figure 3*A*, the ratio of phosphorylated AMPKα to total AMPKα was significantly elevated in ML364-treated mice when compared with vehicle-treated mice ($p = 0.041$; Student's *t* test; $n = 3$; Fig. 3*A*). Hence, inhibition of USP2 augments AMPKα phosphorylation in the VMH. To demonstrate a causal effect of ML364 on neural AMPKα, we detected phosphorylated and total AMPKα in SH-SY5Y cells. Because incubation with 10 μM ML364 for 2 h did not significantly increase LDH content in the culture medium ($p = 0.423$; Student's *t* test; $n = 4$), the concentration of ML364 did not seem to be toxic to SH-SY5Y cells (Fig. 3*B*). Meanwhile, the same concentration of ML364 increased the phosphorylated AMPKα to total AMPKα ratio when compared with vehicle-treated cells ($p = 0.042$; Student's *t* test; $n = 4$; Fig. 3*C*). Therefore, ML364 directly promotes AMPK phosphorylation in neural cells.

As a lack of intracellular ATP stimulates phosphorylation of AMPK (Jeon, 2016), we examined the effects of ML364 on the ATP content of SH-SY5Y cells. As shown in Figure 3*D*, ML364 treatment decreased ATP content by ~64% compared with vehicle-treated cells. Because ATP is mainly supplied by oxidative phosphorylation in neural cells (Rose et al., 2017), we speculated that inhibition of USP2 reduces mitochondrial activity in neural cells. To assess this, we measured the intrinsic enzymatic activities of the respiratory chain complexes in the mitochondria of SH-SY5Y cells. As shown in Figure 3, *E–H*, the activities of complexes I, II, and IV, which contribute to generating proton gradients in mitochondria, were attenuated in ML364-treated cells compared with vehicle-treated cells, except for complex III (complex I, $p = 0.0008$; complex II, $p = 0.023$; complex III, $p = 0.981$; complex IV, $p = 0.003$; Student's *t* test; $n = 3$). Likewise, ML364 also repressed the activity of proton-gradient-driven F_0F_1 ATPase ($p = 0.006$; Student's *t* test; $n = 5$; Fig. 3*I*). Thus, USP2 is likely to sustain mitochondrial respiratory function in SH-SY5Y cells. In agreement with this hypothesis, ML364 lowered the mitochondrial membrane potential, which was assessed through MT-1 staining ($p = 0.001$; Student's *t* test; $n = 4$; Fig. 3*J*). These results collectively indicate that ML364 disrupts mitochondrial complex activity and consequently impairs the ATP supply.

AMPK participates in the hyperglycemia induced after injection of ML364 into the VMH

Next, we examined whether the ML364-elicited AMPK activation contributes to blood glucose elevation. We administrated the AMPK inhibitor CC to the VMH 1 h before ML364 treatment. Two-way ANOVA showed that pretreatment with CC but not ML364 had a significant impact on serum norepinephrine levels ($p = 0.0008$, pretreatment with CC vs vehicle; $p = 0.228$, treatment with ML364 vs vehicle; $F = 13.314$, $p = 0.001$, interaction of both factors; $n = 6$; Fig. 4*A*). *Post hoc* assessment using Tukey's test demonstrated that pretreatment alone with CC did not alter serum norepinephrine levels ($p = 1.000$, vehicle-pretreated, vehicle-treated mice vs CC-pretreated, vehicle-treated mice; $n = 6$; Fig. 4*A*). On the other hand, pretreatment with CC

abolished the increase in circulating norepinephrine after ML364 treatment ($p = 0.005$, vehicle-pretreated, ML364-treated mice vs CC-pretreated, ML364-treated mice; $n = 6$; Fig. 4A). Furthermore, applying CC abrogated the ML364-elicited increases in hepatic glycogen phosphorylase activity and blood glucose levels ($p = 0.0004$ and $p = 0.00007$, Tukey's test; $n = 4$ and $n = 8$; Fig. 4B,C), whereas two-way ANOVA represented significant changes in both indices by pretreatment with CC and treatment with ML364 (glycogen phosphorylase activity; $p = 0.012$, pretreatment with CC vs vehicle; $p = 0.027$; treatment with ML364 vs vehicle, $F = 7.559$, $p = 0.012$, interaction of both factors; $n = 4$; Fig. 4B; blood glucose level, $p = 0.005$ pretreatment with CC vs vehicle; $p = 0.002$; treatment of ML364 vs vehicle; $F = 23.190$, $p = 0.0004$, interaction of both factors; $n = 8$; Fig. 4C). Therefore, AMPK is involved in hyperglycemia after ML364 is injected into the VMH.

ROS accumulation causes the defect in mitochondrial integrity after ML364 treatment

We previously demonstrated that genetic or pharmacological inhibition of USP2 elicited the generation of mitochondrial ROS in cultured myoblasts (Hashimoto et al., 2019). Thus, we speculated that neural cells might exert ROS accumulation after inhibition of USP2. As we anticipated, 2 h treatment with ML364 (10 μM) provoked marked accumulation of ROS in SH-SY5Y cells ($p = 0.00000008$, pretreatment with trolox vs vehicle; $p = 0.002$; treatment with ML364 vs vehicle; $F = 6.056$, $p = 0.023$; interaction with the both indices; two-way ANOVA; $p = 0.000003$, vehicle-pretreated, vehicle-treated cells vs vehicle-pretreated, ML364-treated cells; Tukey's test; $n = 6$; Fig. 5A), which was partially inhibited during pretreatment with 100 μM of trolox ($p = 0.002$, vehicle-pretreated, ML364-treated cells vs trolox-pretreated, ML364-treated cells; $n = 6$; Tukey's test; Fig. 5A). We then assessed whether ROS accumulation was the cause of mitochondrial dysfunction. As shown in Figure 5B, trolox significantly restored the ML364-induced decrease in mitochondrial membrane potential of SH-SY5Y cells ($p = 0.0000000000001$, pretreatment with trolox vs vehicle; $p = 0.0000001$; treatment with ML364 vs vehicle; $F = 67.956$, $p = 0.0000007$; interaction with the both indices; two-way ANOVA; $p = 0.000001$, vehicle-pretreated, ML364-treated cells vs trolox-pretreated, ML364-treated cells; Tukey's test; $n = 6$; Fig. 5B). Simultaneously, trolox mitigated the decrease in intracellular ATP content mediated by ML364 ($p = 0.13$, pretreatment with trolox vs vehicle; $p = 0.0000003$; treatment with ML364 vs vehicle; $F = 5.759$, $p = 0.026$; interaction with the both indices; two-way ANOVA; $p = 0.008$, vehicle-pretreated, ML364-treated cells vs trolox-pretreated, ML364-treated cells; Tukey's test; $n = 6$; Fig. 5C). Similar results of mitochondrial ROS, mitochondrial membrane potential, and intracellular ATP levels were also obtained using 20 mM of NAC as a ROS scavenger (data not shown). These results indicate that ROS accumulation is attributable to the defects of mitochondrial ATP supply in SH-SY5Y cells after ML364 treatment.
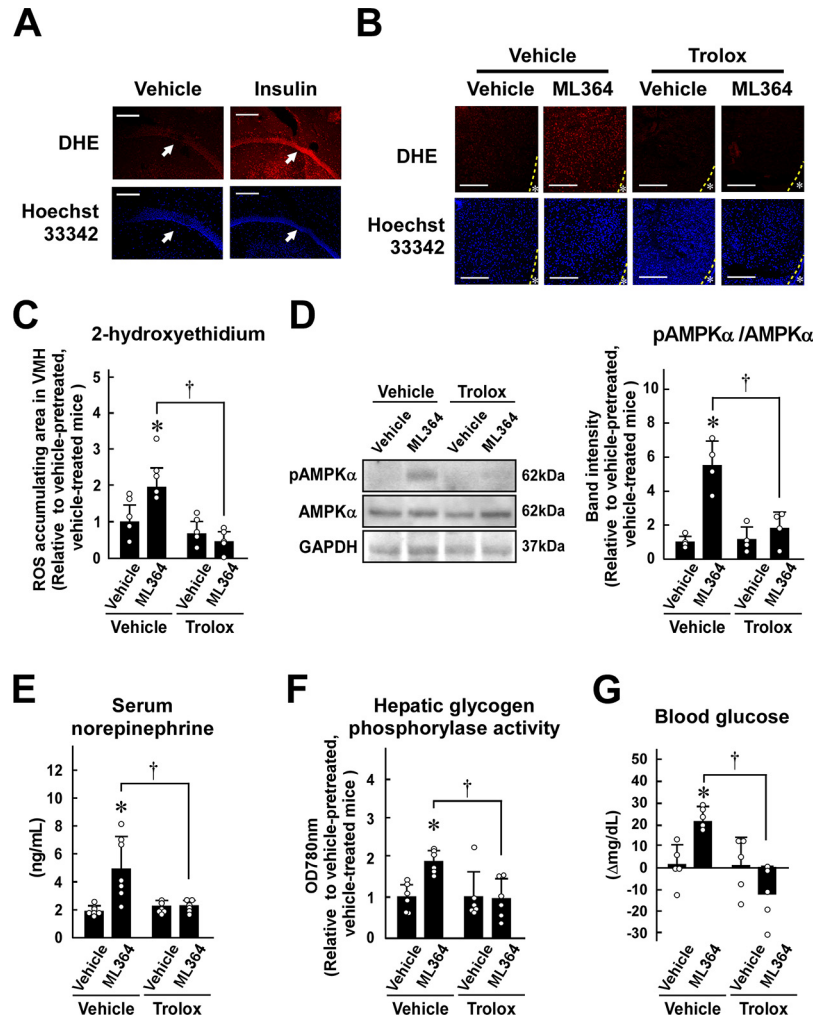

Figure 6. Involvement of hypothalamic ROS accumulation in the ML364-elicited peripheral glucose control. *A*, Brains were collected from mice 30 min after intraperitoneal injection of insulin (1 unit/kg) or vehicle (0.1% BSA-supplemented PBS). Fresh frozen sections were stained with DHE (top) and Hoechst 33342 (bottom), respectively. Scale bar represents 200 μm. *B–G*, Thirty minutes after pretreatment with trolox (50 ng) or vehicle (5% BSA-supplemented PBS) injected into the VMH, ML364 (20 ng) or vehicle (5% BSA-supplemented PBS) was injected to the same region. Brain (*B*, *C*), hypothalamus (*D*), serum (*E*), liver (*F*), and blood (*G*) were collected before (*G*) or 30 min after (*B–G*) administration of either ML364 or vehicle. ROS in the VMH region was detected by DHE (*B*). Brain slice sections were stained with DHE (top) or Hoechst 33342 (bottom). Scale bars represent 200 μm. Stars and dashed lines indicate the third ventricle and its wall, respectively. *C*, The VMH areas showing significant 2-hydroxyethidium-derived fluorescent signal were summed. The mean area of two serial sections was regarded as an area showing ROS accumulation. *D*, Representative blot images (left) for pAMPKα, total AMPKα, and GAPDH in the VMH are shown. Right, Semiquantitative band intensity data are shown. *E–G*, Serum norepinephrine levels (*E*), hepatic glycogen phosphorylase activity (*F*), and blood glucose levels (*G*) were measured. Values are represented as relative to vehicle-pretreated, vehicle-treated mice (*C*, *D*, *F*). Data are shown as mean ± SD of four (*D*), five (*C*, *G*), six (*F*), and seven (*E*) mice. Two-way ANOVA followed by Tukey's test as a *post hoc* test was conducted as statistical analysis (*C–G*); *$p < 0.05$ versus vehicle-treated mice (*C–G*); †$p < 0.05$ versus vehicle-pretreated mice (*C–G*).

ROS accumulation in the VMH contributes to hyperglycemia after injection of ML364 into the VMH

Next, we monitored ROS accumulation in fresh brain sections using the fluorescent ROS indicator DHE. As previously reported (Amador-Alvarado et al., 2014), red fluorescent 2-hydroxyethidium, the oxidized form of DHE, was observed in the DG of the hippocampus after insulin injection, indicating that this experimental protocol works (Fig. 6A). In the hypothalamus, the ROS-elicited red fluorescence was barely visible 30 min after intra-VMH administration of the vehicle (Fig. 6B). In contrast, signal emerged in the VMH after the injection of

ML364 (Fig. 6B). Figure 6C shows a comparison of the VMH area where a significant 2-hydroxyethidium-derived signal was detected. The VMH area of vehicle-pretreated, vehicle-treated; vehicle-pretreated, ML364-treated; trolox-pretreated, vehicle-treated; and trolox-pretreated, ML364-treated mice were 37.1 ± 13.9, 28.3 ± 7.2, 27.6 ± 14.0, and 38.4 ± 14.3 mm^2, respectively ($p = 0.954$, pretreatment with trolox vs vehicle; $p = 0.863$; treatment with ML364 vs vehicle; $F = 3.14$, $p = 0.096$; interaction with the both indices; two-way ANOVA; $n = 5$). Vehicle pretreatment and ML364 treatment provoked ~1.9-fold greater area of ROS-accumulation in the VMH compared with vehicle pretreatment and vehicle treatment ($p = 0.0001$, pretreatment with trolox vs vehicle; $p = 0.067$; treatment with ML364 vs vehicle; $F = 10.01$, $p = 0.006$; interaction with the both indices; two-way ANOVA; $p = 0.011$, vehicle-pretreated, vehicle-treated mice vs vehicle-pretreated, ML364-treated mice; Tukey's test; $n = 5$, Fig. 6C). When we applied trolox (50 ng/head) to the VMH 30 min before ML364 administration, the emersion of 2-hydroxyethidium was completely disrupted, even after ML364 treatment ($p = 0.0002$, vehicle-pretreated, ML364-treated mice vs trolox-pretreated, ML364-treated mice; Tukey's test; $n = 5$; Fig. 6C). Therefore, ML364 stimulates ROS accumulation in the VMH.

We next examined whether ROS mediates the ML364-elicited AMPKα phosphorylation in the mouse VMH. Consistent with the observation that ROS accumulation is less evident in the trolox-pretreated, vehicle-treated mice (Fig. 6B,C), intra-VMH injection of trolox alone did not influence AMPKα phosphorylation in the VMH region ($p = 0.003$, pretreatment with trolox vs vehicle; $p = 0.0001$; treatment with ML364 vs vehicle; $F = 19.826$, $p = 0.003$; interaction with both indices; two-way ANOVA; $p = 0.998$, vehicle-pretreated, vehicle-treated mice vs trolox-pretreated, vehicle-treated mice; Tukey's test; $n = 4$; Fig. 6D). On the other hand, pretreatment with trolox inhibited phosphorylation of AMPKα after ML364 treatment ($p = 0.0007$, vehicle-pretreated, ML364-treated mice vs trolox-pretreated, ML364-treated mice; Tukey's test; $n = 4$; Fig. 6D), whereas pretreatment with vehicle did not have a significant impact on the ML364-induced AMPKα phosphorylation ($p = 0.0001$, vehicle-pretreated, vehicle-treated mice vs vehicle-pretreated, ML364-treated mice; Tukey's test; $n = 4$; Fig. 6D). Therefore, accumulated ROS is responsible for the ML364-induced AMPK phosphorylation in the VMH.

We further appraised whether ROS accumulation in VMH is accompanied with sympathetic activation. As shown in Figure 6E, pretreatment with trolox did not bring about noticeable effects on the serum norepinephrine levels of vehicle-treated mice regardless of pretreatment with trolox or vehicle ($p = 0.008$, pretreatment with trolox vs vehicle; $p = 0.002$; treatment with ML364 vs vehicle; $F = 11.446$, $p = 0.002$; interaction with both indices; two-way ANOVA; $p = 0.983$, trolox-pretreated, vehicle-treated mice vs vehicle-pretreated, vehicle-treated mice; Tukey's test; $n = 7$). In contrast, trolox attenuated the elevation of circulating norepinephrine caused by intra-VMH injection of ML364 ($p = 0.0001$, vehicle-pretreated, ML364-treated mice vs trolox-pretreated, ML364-treated mice; Tukey's test; $n = 7$; Fig. 6E). Thus, ROS provides a dominant contribution to the sympathetic activation after ML364 treatment in the VMH.

Finally, we studied whether the ML364-induced ROS in the VMH consequently activates hepatic glycogen phosphorylase, resulting in the elevation of blood glucose. Even after pretreatment with the vehicle, intra-VMH treatment with ML364 significantly activated hepatic glycogen phosphorylase ($p = 0.028$, pretreatment with trolox vs vehicle; $p = 0.036$; treatment with

ML364 vs vehicle; $F = 6.035$, $p = 0.023$; interaction with both indices; two-way ANOVA; $p = 0.016$, vehicle-pretreated, vehicle-treated mice vs vehicle-pretreated, ML364-treated mice; Tukey's test; $n = 6$; Fig. 6F). In contrast, intra-VMH pretreatment with trolox abated glycogen phosphorylase activity after ML364 treatment ($p = 0.013$, vehicle-pretreated, ML364-treated mice vs trolox-pretreated, ML364-treated mice; Tukey's test; $n = 6$; Fig. 6F). The mean activity of glycogen phosphorylase in trolox-pretreated ML364-treated mice was comparable to vehicle-pretreated, vehicle-treated mice ($p = 0.998$; Tukey's test; $n = 6$; Fig. 6F). Furthermore, trolox pretreatment dampened ML364-induced hyperglycemia ($p = 0.002$, pretreatment with trolox vs vehicle; $p = 0.392$; treatment with ML364 vs vehicle; $F = 11.446$, $p = 0.002$; interaction with both indices; two-way ANOVA; $p = 0.0003$, vehicle-pretreated, ML364-treated mice vs trolox-pretreated, ML364-treated mice; Tukey's test; $n = 5$; Fig. 6G), whereas pretreatment with trolox did not modify blood glucose levels after administration of vehicle instead of ML364 ($p = 1.000$, vehicle-pretreated, vehicle-treated mice vs trolox-pretreated, vehicle-treated mice; Tukey's test; $n = 5$; Fig. 6G). Together, an increment in ROS in the VMH is necessary for glucose mobilization from the liver after hypothalamic ML364 treatment.

Discussion

Previous work reported that USP2 is abundantly expressed in the neurons in the DG of the hippocampus and SCN of the hypothalamus (Scoma et al., 2011; Li et al., 2018). The present study extends the knowledge of the localization of USP2 in the brain. Our ISH proved that *Usp2* mRNA also localizes in several other hypothalamic nuclei, such as the VMH, PVN, and ARC. Moreover, low magnification ISH images of the brain indicated that *Usp2* mRNA signals are distributed in areas where cell bodies of neurons are present in high density. Therefore, USP2 is likely to maintain proper neural activity in a general way. Accordingly, mice lacking *Usp2* exhibited a wide variety of neural defects, including impairments of motor coordination, equilibrium, working memory formation, sensory gating, and anxiety-like behavior, all of which are controlled by distinct brain areas (Srikanta et al., 2021). Given that USP2 is a DUB, the ubiquitination and deubiquitination of certain protein(s) may be a common determinant for neural activity.

In this study, we found that intra-VMH administration of a USP2 inhibitor rapidly elevated blood glucose levels in parallel with an increase in circulating norepinephrine. Although we did not specify the dominant source(s) of the increased serum norepinephrine, the sympathetic nervous system seems to be activated after intra-VMH administration of ML364. Plenty of work has demonstrated that the sympathetic nervous system contributes to glucose mobilization by modifying the function of the liver, muscle, and endocrine tissues (Dubuc et al., 1982; Atrens et al., 1984; Suh et al., 2007; Shiuchi et al., 2009; Güemes and Georgiou, 2018). In the liver, it is well documented that sympathetic activation causes glycogenolysis in a cAMP protein kinase A–dependent pathway (Yang and Yang, 2016). In concert, applying a USP2 inhibitor to the VMH substantially activates hepatic glycogen phosphorylase. Furthermore, statistical correlation analysis in the same cohort study revealed that hyperglycemia after intra-VMH administration of ML364 is related to increased circulating norepinephrine as well as activation of hepatic phosphorylase. Together, USP2 in the VMH may

attenuate sympathetic activation and thereby maintain normal blood glucose levels via the prevention of glycogenolysis.

As reported previously, excessive protein ubiquitination in the hypothalamus was shown to be a determinant of energy expenditure (Susaki et al., 2010). The present study exemplified that an enzyme controlling protein ubiquitination affects glucose mobilization through sympathetic activation. In addition to induction of hyperglycemia, sympathetic activation causes thermogenesis in brown adipose tissue through induction of uncoupled protein 1 (Contreras et al., 2015). Moreover, sympathetic nerves also promote the differentiation of beige adipocytes in subcutaneous white adipose tissues (Richard et al., 2010). Because brown and beige adipocytes consume lipid-stored energy to produce heat, activation of these adipocytes has been proposed as an effective approach for antiobesity therapy (Hanssen et al., 2015; Hankir et al., 2016; Desjardins and Steinberg, 2018). In our preliminary study, intra-VMH treatment of ML364 induced a significant increase of $Ucp1$ expression in the interscapular brown adipose tissue. Thus, USP2 in the VMH might resist metabolic deterioration through activation of brown adipose tissue. A more comprehensive investigation of the sympathoneural function of USP2 will enable us to understand the roles of this DUB in systemic energy homeostasis.

Although chemical inhibition of USP2 in VMH neurons caused hyperglycemia in this study, there have been no reports that genetic knock-outs of $Usp2$ cause elevated blood glucose. As $Usp2$ knock-out mice continuously lack USP2 protein from birth, certain molecular mechanisms may compensate for USP2 deficiency. Another possibility is that $Usp2$ knock-out in other hypothalamic nuclei may counteract the hyperglycemic effects of $Usp2$ knock-out in the VMH. The ARC includes proopiomelanocortin (POMC)-producing neurons (Roh and Kim, 2016), which upregulate hepatic insulin sensitivity and thereby inhibit glycogenolysis and gluconeogenesis in the liver (Dodd et al., 2018). Thus, $Usp2$ knock-out in the POMC neurons may lower blood glucose levels and counteract the hyperglycemia caused by $Usp2$ knock-out in the VMH neurons.

A critical issue of the current study is that the direct target of USP2 in VMH neurons was not identified. In active cells, various biochemical reactions contribute to the accumulation of intracellular ROS. For example, several nicotinamide adenine dinucleotide phosphate oxidases are well known to produce ROS in vasculature and kidney cells, leading to diabetes (Valko et al., 2007). In addition, an imbalance of activities of the mitochondrial respiratory chain complexes also causes ROS accumulation (Kitamura et al., 2008; Lenaz et al., 2010; Yamamori et al., 2012). Specifically, impairments of complexes I and IV cause a surplus of H^+ in mitochondrial intermembrane space, resulting in the accumulation of ROS (Kitamura et al., 2008; Zhao et al., 2019). Thus, USP2 may maintain these ROS-producing machineries directly or indirectly. Another possibility is that USP2 might potentiate the abundance of antioxidants in VMH neurons. So far, some reports have suggested that the ubiquitination of antioxidant proteins determines ROS accumulation in neural cells. For instance, the quantity of peroxiredoxin 1, which is highly expressed in hypothalamic neurons (Wang et al., 2010), is controlled by ubiquitination-dependent degradation (Nasu et al., 2010). Ubiquitination also modulates the stability of hypothalamic glutathione peroxidase 4 (GPX4) (Zhao et al., 2021). Interestingly, GPX4 was decreased in the hypothalamus of high-fat-fed and high-sucrose-fed obese mice (Schriever et al., 2017). Therefore, USP2 might stabilize such antioxidant

proteins, resulting in mitigation of ROS accumulation in the VMH. Further studies are needed to clarify USP2 targets that maintain neural activity in the VMH.

Growing evidence shows that hypothalamic ROS is responsible for systemic metabolic disorder. Mitochondrial ROS in hypothalamus neurons was proved to be closely associated with metabolic disturbances in type 2 diabetic mice (Colombani et al., 2009). Moreover, the amount of hypothalamic ROS represents a positive correlation with hepatic glucose synthesis and plasma norepinephrine levels, both of which are remarkably increased in type 2 diabetic patients (Gyengesi et al., 2012; Drougard et al., 2014, 2015). In this study, we suggest that inhibition of USP2 causes marked accumulation of ROS in VMH neurons, followed by changes in glucose mobilization in mice. Hence, diabetic patients might display aberrant activation of USP2 in the VMH.

The current study shows that USP2 inhibition causes AMPKα phosphorylation via ROS accumulation in the VMH. However, we did not uncover the molecular mechanism underlying the ROS-elicited AMPK phosphorylation. Because oxidation of the C299 or C304 residues of AMPKα promotes phosphorylation of AMPKα (Zmijewski et al., 2010), ROS may directly activate AMPKα after intra-VMH administration of ML364. In addition, the phosphorylation status of AMPKα is also determined by the ratio of intracellular ATP/ADP (Ke et al., 2018); a decrease of the ATP/ADP ratio potentiates AMPKα phosphorylation (Carling, 2017). In this study, ML364-evoked ROS accumulation prevented ATP supply from mitochondria in SH-SY5Y cells. Thus, prevention of mitochondrial ATP synthesis might be a major course of AMPKα phosphorylation after intra-VMH administration of ML364.

Although intra-VMH treatment of trolox abrogated ML364-provoked ROS accumulation in the mouse hypothalamus, the effect of trolox or NAC on the ROS level was partial in SH-SY5Y cells. ROS might be more extensively produced in the cultured neural cells than the hypothalamic neuron. Actually, neural progenitor cells sustain high redox status to maintain proliferative activity (Staerk et al., 2010; Xie et al., 2015). Thus, complete depletion of intracellular ROS might be more difficult in SH-SY5Y cells than differentiated neurons in the hypothalamus.

In the present study, we injected ML364 into the VMH as a means of mitigating USP2 activity in this nucleus. In terms of circulating glucose control, the inhibitory effects of ML364 are likely to be specific to the VMH as the application of ML364 into adjacent areas did not give significant increases in blood glucose levels compared with VMH. However, we still cannot exclude the possibility that ML364 affects other USPs in the VMH, resulting in sympathetic activation, although ML364 has been proven to be a selective inhibitor of USP2 (Davis et al., 2016; Hashimoto et al., 2019; Zhang et al., 2020). Therefore, a combinatory evaluation using genetic and pharmacological techniques is desirable. Because the steroidogenic factor 1 ($Sf1$) gene promoter preferably acts in VMH neurons (Dhillon et al., 2006; Toda et al., 2016), a phenotypic analysis of $Usp2$ conditional knock-out mice (offspring of $Usp2^{fl/fl}$ mice and $Sf1$-Cre mice) may strengthen the idea that USP2 in the VMH has glucoregulatory roles through the control of sympathetic nervous activation.

In conclusion, we found that USP2 controls AMPK, resulting in modification of blood glucose levels. Because AMPK in the VMH has been proposed to be responsible for the set point of circulating glucose level, this study provides a novel cue to modulate basal glucose metabolism. Ubiquitination and deubiquitination are reversible and rapid enzymatic processes. Thus, these processes seem to be suitable to maintain brain physiological

function under dynamic environmental changes. Although USP2 deubiquitinates a wide variety of proteins (Kitamura and Hashimoto, 2021), structures of USP2-containing protein complex are known to be a determinant for its targets (Yang et al., 2014). In this sense, augmentation of the adequate protein complex formation in VMH neurons might confer a novel strategy for hyperglycemic therapy.

References

Amador-Alvarado L, Montiel T, Massieu L (2014) Differential production of reactive oxygen species in distinct brain regions of hypoglycemic mice. Metab Brain Dis 29:711–719.

Atrens DM, Sinden JD, Pénicaud L, Louis-Sylvestre J, Le Magnen J (1984) The effect of electrical stimulation of the hypothalamus on continuously-monitored blood glucose levels. Physiol Behav 33:537–542.

Berthoud HR, Morrison C (2008) The brain, appetite, and obesity. Annu Rev Psychol 59:55–92.

Carling D (2017) AMPK signalling in health and disease. Curr Opin Cell Biol 45:31–37.

Castañeda-Cabral JL, López-Ortega JG, Fajardo-Fregoso BF, Beas-Zárate C, Ureña-Guerrero ME (2020) Glutamate induced neonatal excitotoxicity modifies the expression level of EAAT1 (GLAST) and EAAT2 (GLT-1) proteins in various brain regions of the adult rat. Neurosci Lett 735:135237.

Chuang SJ, Cheng SC, Tang HC, Sun CY, Chou CY (2018) 6-Thioguanine is a noncompetitive and slow binding inhibitor of human deubiquitinating protease USP2. Sci Rep 8:3102.

Colombani AL, Carneiro L, Benani A, Galinier A, Jaillard T, Duparc T, Offer G, Lorsignol A, Magnan C, Casteilla L, Pénicaud L, Leloup C (2009) Enhanced hypothalamic glucose sensing in obesity: alteration of redox signaling. Diabetes 58:2189–2197.

Contreras C, Gonzalez F, Fernø J, Diéguez C, Rahmouni K, Nogueiras R, López M (2015) The brain and brown fat. Ann Med 47:150–168.

Coutinho EA, Okamoto S, Ishikawa AW, Yokota S, Wada N, Hirabayashi T, Saito H, Sato T, Takagi K, Wang CC, Kobayashi K, Ogawa Y, Shioda S, Yoshimura Y, Minokoshi Y (2017) Activation of SF1 neurons in the ventromedial hypothalamus by DREADD technology increases insulin sensitivity in peripheral tissues. Diabetes 66:2372–2386.

Davis MI, Pragani R, Fox JT, Shen M, Parmar K, Gaudiano EF, Liu L, Tanega C, McGee L, Hall MD, McKnight C, Shinn P, Nelson H, Chattopadhyay D, D'Andrea AD, Auld DS, Delucas L, Li Z, Boxer MB, Simeonov A (2016) Small molecule inhibition of the ubiquitin-specific protease USP2 accelerates cyclin D1 degradation and leads to cell cycle arrest in colorectal cancer and mantle cell lymphoma models. J Biol Chem 291:24628–24640.

Desjardins EM, Steinberg GR (2018) Emerging role of AMPK in brown and beige adipose tissue (BAT): implications for obesity, insulin resistance, and type 2 diabetes. Curr Diab Rep 18:80.

Dhillon H, Zigman JM, Ye C, Lee CE, McGovern RA, Tang V, Kenny CD, Christiansen LM, White RD, Edelstein EA, Coppari R, Balthasar N, Cowley MA, Chua S Jr, Elmquist JK, Lowell BB (2006) Leptin directly activates SF1 neurons in the VMH, and this action by leptin is required for normal body-weight homeostasis. Neuron 49:191–203.

Dodd GT, Michael NJ, Lee-Young RS, Mangiafico SP, Pryor JT, Munder AC, Simonds SE, Claus J, Ning B, Zhang Z-Y, Cowley MA, Andrikopoulos S, Horvath TL, Spanswick D, Tiganis T (2018) Insulin regulates POMC neuronal plasticity to control glucose metabolism. Elife 7:e38704.

Drougard A, Duparc T, Brenachot X, Carneiro L, Gouazé A, Fournel A, Geurts L, Cadoudal T, Prats AC, Pénicaud L, Vieau D, Lesage J, Leloup C, Benani A, Cani PD, Valet P, Knauf C (2014) Hypothalamic apelin/reactive oxygen species signaling controls hepatic glucose metabolism in the onset of diabetes. Antioxid Redox Signal 20:557–573.

Drougard A, Fournel A, Valet P, Knauf C (2015) Impact of hypothalamic reactive oxygen species in the regulation of energy metabolism and food intake. Front Neurosci 9:1–12.

Dubuc PU, Leshin LS, Willis PL (1982) Glucose and endocrine responses to hypothalamic electrical stimulation in rats. Am J Physiol 242:R220–R226.

Finley J (2019) Cellular stress and AMPK links metformin and diverse compounds with accelerated emergence from anesthesia and potential recovery from disorders of consciousness. Med Hypotheses 124:42–52.

Fryer LGD, Carling D (2005) AMP-activated protein kinase and the metabolic syndrome. Biochem Soc Trans 33:362–366.

Gagnidze K, Weil ZM, Faustino LC, Schaafsma SM, Pfaff DW (2013) Early histone modifications in the ventromedial hypothalamus and preoptic area following oestradiol administration. J Neuroendocrinol 25:939–955.

Gousseva N, Baker RT (2003) Gene structure, alternate splicing, tissue distribution, cellular localization, and developmental expression pattern of mouse deubiquitinating enzyme isoforms Usp2-45 and Usp2-69. Gene Expr 11:163–179.

Güemes A, Georgiou P (2018) Review of the role of the nervous system in glucose homoeostasis and future perspectives towards the management of diabetes. Bioelectron Med 4:9.

Gyengesi E, Paxinos G, Andrews ZB (2012) Oxidative stress in the hypothalamus: the importance of calcium signaling and mitochondrial ROS in body weight regulation. Curr Neuropharmacol 10:344–353.

Hankir MK, Cowley MA, Fenske WK (2016) A BAT-centric approach to the treatment of diabetes: turn on the brain. Cell Metab 24:31–40.

Hanssen MJW, Hoeks J, Brans B, Lans AAJJ, Schaart G, van den Driessche JJ, Jörgensen JA, Boekschoten M, Hesselink MKC, Havekes B, Kersten S, Mottaghy FM, Marken Lichtenbelt WD, Schrauwen P (2015) Short-term cold acclimation improves insulin sensitivity in patients with type 2 diabetes mellitus. Nat Med 21:863–865.

Hashimoto M, Saito N, Ohta H, Yamamoto K, Tashiro A, Nakazawa K, Inanami O, Kitamura H (2019) Inhibition of ubiquitin-specific protease 2 causes accumulation of reactive oxygen species, mitochondria dysfunction, and intracellular ATP decrement in C2C12 myoblasts. Physiol Rep 7:e14193.

Hashimoto M, Kimura S, Kanno C, Yanagawa Y, Watanabe T, Okabe J, Takahashi E, Nagano M, Kitamura H (2021) Macrophage ubiquitin-specific protease 2 contributes to motility, hyperactivation, capacitation, and in vitro fertilization activity of mouse sperm. Cell Mol Life Sci 78:2929–2948.

He J, Lee HJ, Saha S, Ruan D, Guo H, Chan CH (2019) Inhibition of USP2 eliminates cancer stem cells and enhances TNBC responsiveness to chemotherapy. Cell Death Dis 10:285.

Hinchy EC, Gruszczyk AV, Willows R, Navaratnam N, Hall AR, Bates G, Bright TP, Krieg T, Carling D, Murphy MP (2018) Mitochondria-derived ROS activate AMP-activated protein kinase (AMPK) indirectly. J Biol Chem 293:17208–17217.

Hirschberg PR, Sarkar P, Teegala SB, Routh VH, New R (2020) Ventromedial hypothalamus glucose-inhibited neurones: a role in glucose and energy homeostasis? J Neuroendocrinol 32:e12773.

Ikegami M, Ikeda H, Ohashi T, Ohsawa M, Ishikawa Y, Kai M, Kamei A, Kamei J (2013) Olanzapine increases hepatic glucose production through the activation of hypothalamic adenosine 5′-monophosphate-activated protein kinase. Diabetes Obes Metab 15:1128–1135.

Jeon SM (2016) Regulation and function of AMPK in physiology and diseases. Exp Mol Med 48:e245.

Kalsbeek A, Bruinstroop E, Yi CX, Klieverik LP, La Fleur SE, Fliers E (2010) Hypothalamic control of energy metabolism via the autonomic nervous system. Ann N Y Acad Sci 1212:114–129.

Ke R, Xu Q, Li C, Luo L, Huang D (2018) Mechanisms of AMPK in the maintenance of ATP balance during energy metabolism. Cell Biol Int 42:384–392.

Kitamura H, Hashimoto M (2021) Molecular sciences USP2-related cellular signaling and consequent pathophysiological outcomes. Int J Mol Sci 22:1209.

Kitamura H, Ito M, Yuasa T, Kikuguchi C, Hijikata A, Takayama M, Kimura Y, Yokoyama R, Kaji T, Ohara O (2008) Genome-wide identification and characterization of transcripts translationally regulated by bacterial lipopolysaccharide in macrophage-like J774.1 cells. Physiol Genomics 33:121–132.

Kitamura H, Kimura S, Shimamoto Y, Okabe J, Ito M, Miyamoto T, Naoe Y, Kikuguchi C, Meek B, Toda C, Okamoto S, Kanehira K, Hase K, Watarai H, Ishizuka M, El-Osta A, Ohara O, Miyoshi I (2013) Ubiquitin-specific protease 2-69 in macrophages potentially modulates metainflammation. FASEB J 27:4940–4953.

Kitamura H, Ishino T, Shimamoto Y, Okabe J, Miyamoto T, Takahashi E, Miyoshi I (2017) Ubiquitin-specific protease 2 modulates the lipopolysaccharide-elicited expression of proinflammatory cytokines in macrophage-like HL-60 cells. Mediators Inflamm 2017:6909415.

Konno K, Matsuda K, Nakamoto C, Uchigashima M, Miyazaki T, Yamasaki M, Sakimura K, Yuzaki M, Watanabe M (2014) Enriched expression of GluD1 in higher brain regions and its involvement in parallel fiber-interneuron synapse formation in the cerebellum. J Neurosci 34:7412–7424.

Lenaz G, Baracca A, Barbero G, Bergamini C, Dalmonte ME, Del Sole M, Faccioli M, Falasca A, Fato R, Genova ML, Sgarbi G, Solaini G (2010) Mitochondrial respiratory chain super-complex I-III in physiology and pathology. Biochim Biophys Acta 1797:633–640.

Li C, Zhang J, Xu H, Chang M, Lv C, Xue W, Song Z, Zhang L, Zhang X, Tian X (2018) Retigabine ameliorates acute stress-induced impairment of spatial memory retrieval through regulating USP2 signaling pathways in hippocampal CA1 area. Neuropharmacology 135:151–162.

Liu H, Xu Y, Hu F (2020) AMPK in the ventromedial nucleus of the hypothalamus: a key regulator for thermogenesis. Front Endocrinol (Lausanne) 11:578830.

Magiera K, Tomala M, Kubica K, de Cesare V, Trost M, Zieba BJ, Kachamakova-Trojanowska N, Les M, Dubin G, Holak TA, Skalniak L (2017) Lithocholic acid hydroxyamide destabilizes cyclin D1 and induces G0/G1 arrest by inhibiting deubiquitinase USP2a. Cell Chem Biol 24:458–470.e18.

Mastaitis JW, Wurmbach E, Cheng H, Sealfon SC, Mobbs CV (2005) Acute induction of gene expression in brain and liver by insulin-induced hypoglycemia. Diabetes 54:952–958.

Meek TH, Nelson JT, Matsen ME, Dorfman MD, Guyenet SJ, Damian V, Allison MB, Scarlett JM, Nguyen HT, Thaler JP, Olson DP, Myers MG, Schwartz MW, Morton GJ (2016) Functional identification of a neurocircuit regulating blood glucose. Proc Natl Acad Sci U S A 113:E2073–E2082.

Mo J, Enkhjargal B, Travis ZD, Zhou K, Wu P, Zhang G, Zhu Q, Zhang T, Peng J, Xu W, Ocak U, Chen Y, Tang J, Zhang J, Zhang JH (2019) AVE 0991 attenuates oxidative stress and neuronal apoptosis via Mas/PKA/CREB/UCP-2 pathway after subarachnoid hemorrhage in rats. Redox Biol 20:75–86.

Nasu J, Murakami K, Miyagawa S, Yamashita R, Ichimura T, Wakita T, Hotta H, Miyamura T, Suzuki T, Satoh T, Shoji I (2010) E6AP ubiquitin ligase mediates ubiquitin-dependent degradation of peroxiredoxin 1. J Cell Biochem 111:676–685.

Priolo C, Tang D, Brahamandan M, Benassi B, Sicinska E, Ogino S, Farsetti A, Porrello A, Finn S, Zimmermann J, Febbo P, Loda M (2006) The isopeptidase USP2a protects human prostate cancer from apoptosis. Cancer Res 66:8625–8632.

Richard D, Carpentier AC, Doré G, Ouellet V, Picard F (2010) Determinants of brown adipocyte development and thermogenesis. Int J Obes (Lond) 2:S59–S66.

Roh E, Kim MS (2016) Brain regulation of energy metabolism. Endocrinol Metab (Seoul) 31:519–524.

Rose J, Brian C, Woods J, Pappa A, Panayiotidis MI, Powers R, Franco R (2017) Mitochondrial dysfunction in glial cells: Implications for neuronal homeostasis and survival. Toxicology 391:109–115.

Schneider CA, Rasband WS, Eliceiri KW (2012) NIH Image to ImageJ: 25 years of image analysis. Nat Methods 9:671–675.

Schriever SC, Zimprich A, Pfuhlmann K, Baumann P, Giesert F, Klaus V, Kabra DG, Hafen U, Romanov A, Tschöp MH, Wurst W, Conrad M, Hölter SM, Vogt Weisenhorn D, Pfluger PT (2017) Alterations in neuronal control of body weight and anxiety behavior by glutathione peroxidase 4 deficiency. Neuroscience 357:241–254.

Scoma HD, Humby M, Yadav G, Zhang Q, Fogerty J, Besharse JC (2011) The de-ubiquitinylating enzyme, USP2, is associated with the circadian clockwork and regulates its sensitivity to light. PLoS One 6:e25382.

Seoane-Collazo P, Fernø J, Gonzalez F, Diéguez C, Leis R, Nogueiras R, López M (2015) Hypothalamic-autonomic control of energy homeostasis. Endocrine 50:276–291.

Shanmughapriya S, et al. (2015) SPG7 Is an essential and conserved component of the mitochondrial permeability transition pore. Mol Cell 60:47–62.

Shi Y, Solomon LR, Pereda-Lopez A, Giranda VL, Luo Y, Johnson EF, Shoemaker AR, Leverson J, Liu X (2011) Ubiquitin-specific cysteine protease 2a (USP2a) regulates the stability of Aurora-A. J Biol Chem 286:38960–38968.

Shibata T, Yamada K, Watanabe M, Ikenaka K, Wada K, Tanaka K, Inoue Y (1997) Glutamate transporter GLAST is expressed in the radial glia-astrocyte lineage of developing mouse spinal cord. J Neurosci 17:9212–9219.

Shimazu T (1981) Central nervous system regulation of liver and adipose tissue metabolism. Diabetologia 20:343–356.

Shiuchi T, Haque MS, Okamoto S, Inoue T, Kageyama H, Lee S, Toda C, Suzuki A, Bachman ES, Kim YB, Sakurai T, Yanagisawa M, Shioda S, Imoto K, Minokoshi Y (2009) Hypothalamic orexin stimulates feeding-associated glucose utilization in skeletal muscle via sympathetic nervous system. Cell Metab 10:466–480.

Srikanta SB, Stojkovic K, Cermakian N (2021) Behavioral phenotyping of mice lacking the deubiquitinase USP2. PLoS One 16:e0241403–17.

Staerk J, Dawlaty MM, Gao Q, Maetzel D, Hanna J, Sommer CA, Mostoslavsky G, Jaenisch R (2010) Reprogramming of human peripheral blood cells to induced pluripotent stem cells. Cell Stem Cell 7:20–24.

Suh SH, Paik IY, Jacobs KA (2007) Regulation of blood glucose homeostasis during prolonged exercise. Mol Cells 23:272–279.

Susaki E, Kaneko-Oshikawa C, Miyata K, Tabata M, Yamada T, Oike Y, Katagiri H, Nakayama KI (2010) Increased E4 activity in mice leads to ubiquitin-containing aggregates and degeneration of hypothalamic neurons resulting in obesity. J Biol Chem 285:15538–15547.

Swatek KN, Komander D (2016) Ubiquitin modifications. Cell Res 26:399–422.

Tanida M, Yamamoto N, Morgan DA, Kurata Y, Shibamoto T, Rahmouni K (2015) Leptin receptor signaling in the hypothalamus regulates hepatic autonomic nerve activity via phosphatidylinositol 3-kinase and AMP-activated protein kinase. J Neurosci 35:474–484.

Toda C, Kim JD, Impellizzeri D, Cuzzocrea S, Liu ZW, Diano S (2016) UCP2 regulates mitochondrial fission and ventromedial nucleus control of glucose responsiveness. Cell 164:872–883.

Tomala MD, Magiera-Mularz K, Kubica K, Krzanik S, Zieba B, Musielak B, Pustula M, Popowicz GM, Sattler M, Dubin G, Skalniak L, Holak TA (2018) Identification of small-molecule inhibitors of USP2a. Eur J Med Chem 150:261–267.

Valko M, Leibfritz D, Moncol J, Cronin MTD, Mazur M, Telser J (2007) Free radicals and antioxidants in normal physiological functions and human disease. Int J Biochem Cell Biol 39:44–84.

Wang QM, Cai Y, Tian DR, Yang H, Wei ZN, Wang F, Han JS (2010) Peroxiredoxin1: A potential obesity-related factor in the hypothalamus. Med Sci Monit 16:321–326.

Xie W, Wang JQ, Wang QC, Wang Y, Yao S, Tang TS (2015) Adult neural progenitor cells from Huntington's disease mouse brain exhibit increased proliferation and migration due to enhanced calcium and ROS signals. Cell Prolif 48:517–531.

Yamamori T, Yasui H, Yamazumi M, Wada Y, Nakamura Y, Nakamura H, Inanami O (2012) Ionizing radiation induces mitochondrial reactive oxygen species production accompanied by upregulation of mitochondrial electron transport chain function and mitochondrial content under control of the cell cycle checkpoint. Free Radic Biol Med 53:260–270.

Yang H, Yang L (2016) Targeting cAMP/PKA pathway for glycemic control and type 2 diabetes therapy. J Mol Endocrinol 57:R93–R108.

Yang Y, Duguay D, Fahrenkrug J, Cermakian N, Wing SS (2014) USP2 regulates the intracellular localization of PER1 and circadian gene expression. J Biol Rhythms 29:243–256.

Zhang J, Liu S, Li Q, Shi Y, Wu Y, Liu F, Wang S, Zaky MY, Yousuf W, Sun Q, Guo D, Wang T, Zhang Y, Wang Y, Li M, Liu H (2020) The deubiquitylase USP2 maintains ErbB2 abundance via counteracting endocytic degradation and represents a therapeutic target in ErbB2-positive breast cancer. Cell Death Differ 27:2710–2725.

Zhao L, Gong H, Huang H, Tuerhong G, Xia H (2021) Participation of mind bomb-2 in sevoflurane anesthesia induces cognitive impairment in aged mice via modulating ferroptosis. ACS Chem Neurosci 12:2399–2408.

Zhao RZ, Jiang S, Zhang L, Yu Z (2019) Mitochondrial electron transport chain, ROS generation and uncoupling (Review). Int J Mol Med 44:3–15.

Zhao Y, et al. (2018) USP2a supports metastasis by tuning TGF-β signaling. Cell Rep 22:2442–2454.

Zmijewski JW, Banerjee S, Bae H, Friggeri A, Lazarowski ER, Abraham E (2010) Exposure to hydrogen peroxide induces oxidation and activation of AMP-activated protein kinase. J Biol Chem 285:33154–33164.